Nanopaper-Based Organic Inkjet-Printed Diodes

Silvia Conti, Carme Martínez-Domingo, Makara Lay, Lluís Terés, Fabiola Vilaseca, and Eloi Ramon**

The rise of internet of things (IoTs) applications has led to the development of a new generation of light-weight, flexible, and cost-effective electronics. These devices and sensors have to be simultaneously easily replaceable and disposable while being environmentally sustainable. Thus, the introduction of new functionalized materials with mechanical flexibility that can be processed using large-area and facile fabrication methods (as, for example, printing technologies) has become a matter of great interest in the scientific community. In this context, cellulose nanofibers (CNFs) are renewable, affordable, robust, and nontoxic materials that are rapidly emerging as components for eco-friendly electronics. Their combination with conductive polymers (CPs) to obtain conductive nanopapers (CNPs) allows moving their functionality from just substrates to active components of the device. In this work, a route for the inkjet-printing of organic diodes is outlined. The proposed strategy is based on the use of CNPs as both substrates and bottom electrodes onto which insulator and organic semiconducting layers are deposited to fabricate novel diode structures. Remarkable rectification ratios of up to 1.2×10^3 at |3 V| and a current density up to 5.1 µA cm^{-2} are achieved. As a proof-of-concept of the potentiality of the approach for versatile, low-temperature, and disposable sensing applications, an NO_2 gas sensor is presented.

1. Introduction

The growing demand of flexible electronic devices for the development of the internet of things (IoTs) applications is expected to lead to an increase in the amount of nonbiodegradable solid waste and plastic litter with obvious negative consequences for the environment.[1–3] Introducing biocompatibility, reusability, and, eventually, biodegradability to consumer electronics will alleviate the environmental issues and significantly reduce the costs associated with recycling operations. Paper-based electronics is a rising technology that offers great advantages such as bendability, ease of recycling/disposal, and cost-efficiency.[4,5] Derived from abundant and renewable raw materials, and thanks to their outstanding physical, chemical, and mechanical properties, cellulose nanofibers (CNFs) represent one of the most promising components for the production of sustainable, biodegradable, and eco-friendly electronics.[6–8] However, most of the works reported so far address the use of these materials just as substrates for functional electronic components.[9] Nevertheless, CNFs can work as both substrates and active components for the fabrication of devices and sensors.[10–13] In 2014, for example, Gaspar et al.[14] presented a nanopaper-based field effect transistor (FET) fabricated using cotton-based nanocrystalline cellulose (NCC) as the substrate and as the gate dielectric layer, building the device on both sides of the NCC films. Following the same idea, Dai et al.[15] more recently reported on the use of cellulose nanopapers (CNPs) as high-capacitance all-solid dielectrics for flexible and low-voltage Organic FETs. Tammela et al.[16] demonstrated the use of polypyrrole (PPy) coated nanocellulose composites as electrodes for the fabrication of asymmetric supercapacitor

Dr. S. Conti
Dipartimento di Ingegneria dell'Informazione
University of Pisa
56122 Pisa, Italy

Dr. S. Conti, Dr. C. Martínez-Domingo, Prof. L. Terés, Prof. E. Ramon
ICAS Group
Institute of Microelectronics of Barcelona
IMB-CNM (CSIC)
Cerdanyola del Vallès, 08193 Barcelona, Spain
E-mail: carme.martinez@imb-cnm.csic.es; eloi.ramon@imb-cnm.csic.es

The ORCID identification number(s) for the author(s) of this article can be found under https://doi.org/10.1002/admt.201900773.

DOI: 10.1002/admt.201900773

Dr. M. Lay
Laboratory of Organic Electronic
Department of Science and Technology
Linköping University
SE-601 74 Norrköping, Sweden

Prof. F. Vilaseca
Advanced Biomaterials and Nanotechnology (BIMATEC Group)
Department of Chemical Engineering
Agricultural and Food Technology
University of Girona
c/M. Aurèlia Capmany 61, 17003 Girona, Spain

Prof. F. Vilaseca
Department of Fiber and Polymer Tecnology
KTH Royal Institute of Technology
SE-114 28 Stockholm, Sweden

cells. Thanks to their 3D porous structure, CNFs can easily accommodate functional materials, allowing to reduce the complexity of the fabrication processes and to overcome electrode adhesion problems, often detrimental, for the performance and durability of the devices. On the other hand, they are characterized by heterogeneous chemical and physical features and thus can be challenging when employed in electronics.[17] One of the main problems is represented by their high surface roughness and porosity, it's negative influence on device's electrical performance, such as hysteresis, bad injection current, and high gate leakage current, has been widely reported in the literature.[18–21] Another limiting aspect of using CNPs is the moderate processing temperature compatible with these substrates.[22,23] In order to deal with these issues, organic materials and inkjet-printing were chosen as the device's components and deposition technique because the former do not require high-temperature deposition and are compatible with large-area production and solution-based processes,[24] while the latter has proven to be a suitable technology for the deposition of smooth thin layers.[25] Moreover, inkjet-printing is a versatile, low-material, low-time, and low-power consuming approach.[26,27]

In this paper, starting from our previous works,[28–30] different conductive polymers (CPs) such as poly(3,4-ethylenedioxythiophene):poly(styrene sulfonates) (PEDOT:PSS), PPy and multi-walled carbon nanotubes (MWCNTs) were combined with CNFs for the preparation of CNPs, that were used as environmentally friendly portable substrates/electrodes for the fabrication of diode structures. In this sense, these CPs have gained a lot of attention over the years as attractive candidates to replace inorganic conductors. In particular, the herein selected CPs allow in situ polymerization,[31] that exhibit good intrinsic conductivity,[32] and it is possible to easily tune their properties by chemistry.[33] Furthermore, MWCNTs were favored because of their outstanding mechanical properties and high electrical conductivities, which can be used to improve substantially the electrical conductivity of CNFs.[34–36]

Diodes are two-terminal electronic devices which present asymmetric current–voltage (*I*–*V*) characteristics and rectifying behaviors. The key component of a diode is the interface that permits the current to flow in one direction but not in the other. Our group recently proposed a novel polymeric rectifier based on inkjet-printed metal-insulator-semiconductor (MIS) structure fabricated onto plastic substrate.[37] Unlike the conventional Schottky barrier diode, this structure relies on the insertion of a leaky inkjet-printed insulator between the metallic bottom electrode (BE) and the organic semiconductor (OSC) that creates the energy barrier responsible for the rectifying behavior. Since the rectification does not depend on the BE/OSC interface, the inkjet-printed metallic BE was replaced by CNPs, acting both as the electrode and as the substrate as shown in **Figure 1**. As in our previous work,[37] crosslinked poly(4-vinylphenol) (cPVP),[25] an epoxy resin (Priélex, PLX),[38] and an high-K epoxy resin with amorphous silica (UTDots)[39] were used as the insulating layer, and Merck SP400 was chosen as the amorphous p-type OSC. This work improves the device characteristics in terms of costs, degradability, and electrical performances. Best results were obtained for one type of PEDOT:PSS doped nanopapers that showed a degradability of 100% upon exposure to a common electrolytic environment for 2 days, and rectification ratios (RRs) of up to 1.2×10^3 at |3| V. Finally, the proposed diode was used to develop a proof-of-concept room temperature gas sensor as a first example of the possible applications of these structures.

2. Results and Discussion

Figure 1a shows the fabrication scheme of the diodes, while Figure 1b presents an optical image and a scanning electron microscopy (SEM) image of one of the devices. As underlined in the introduction, this approach is based on the use of CNPs as both substrates and bottom electrodes of the diodes. A leaky dielectric between the electrode and the semiconductor is responsible for the creation of an energy barrier that allows the current to flow just in one direction and gives the asymmetric current–voltage characteristic typical of a diode. Different combinations of CNPs and insulating polymers have been evaluated.

2.1. Nanopaper Characterization

It is possible to change the electrical behavior of nanocellulose from insulating to semiconductive and, eventually, conductive

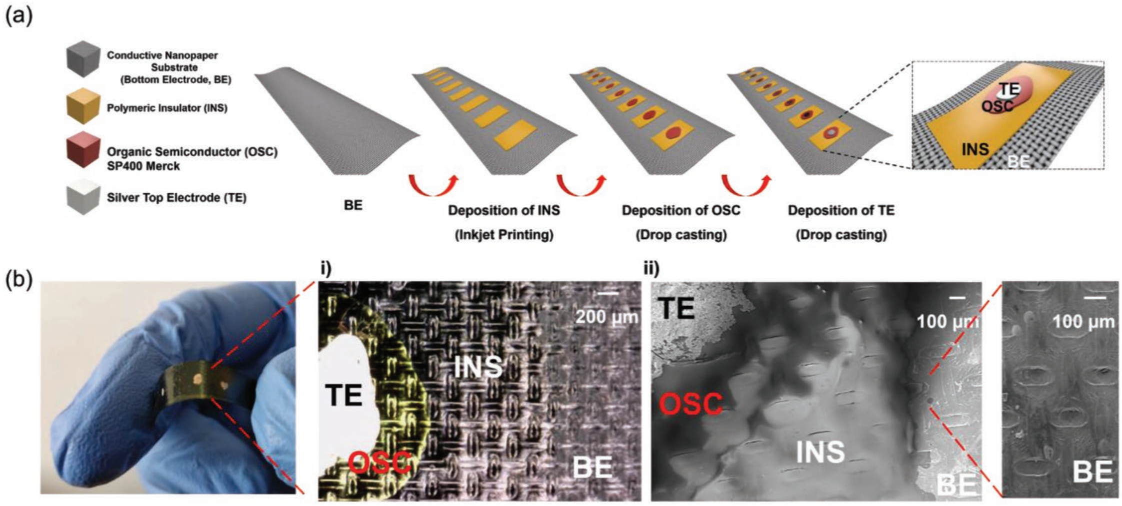

Figure 1. a) Fabrication scheme of the diode structures. b) i) Optical and ii) SEM images of $PT2_{50}$/UTDots diodes.

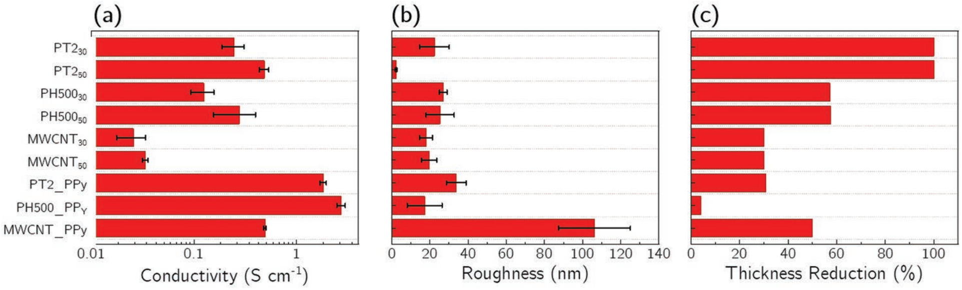

Figure 2. a) Conductivities, b) RMSR values, and c) thickness reduction percentages of the different CNPs.

through its combination with conductive materials. **Figure 2**a shows the electrical conductivities of the all different CNP formulations. A scheme of the composition of the different CNP formulation is shown in Figure S1 in the Supporting Information. The chemical structure of the CPs employed for the preparation of the CNPs is reported in Figure S2 in the Supporting Information. From a general comparison between the two PEDOT:PSS groups, one can notice that nanopapers containing PT2 were slightly more conductive than the ones based on PH500, even if the latter presented a higher intrinsic conductivity (80 and 300 S cm^{-1}, respectively) and a higher surface area.[30] The lowering of the PH500 group's conductivities can be related to the formation of agglomerates that might result in an inhomogeneous distribution of the polymer into the CNPs, as confirmed by the root mean square roughness (RMSR) values extracted from the atomic force microscopy (AFM) analysis (see Figure 2b, Figure S3, Supporting Information). MWCNTs CNPs present the lower conductivity value achieved in this work (≈0.03 S cm^{-1}). This value is considerably low in comparison with the metallic-like electrical conductivity of pristine MWCNTs.[28] Acid modification treatment of the MWCNT during the nanocellulose preparation may provoke defects on the MWCNTs sidewall. The hopping of charges in between carbon nanotubes and around defects, which can be eventually present in the bulk, is responsible for the reduction in the electrical conductivity.[40]

Rough substrate creates trap states and molecular disorders in the organic interfaces that dramatically decrease the OSC's mobility and produce short circuits through the device. In order to have good electrical performances of the devices, a substrate roughness in the range of 2–8 nm is desired.[41,42] Thus, $PT2_{30}$ CNPs are very suitable as substrates due to their extremely smooth surface of around 2 nm RMSR, which is comparable with planarized plastic substrates.[43] For PH500 group, an increase of its solid content from 30 to 50 wt% did not imply a noticeable increase of surface roughness. The same behavior was obtained for MWCNT group.

Composite materials of MWCNTs and CPs have attracted great interest because they often present characteristics superior to either of the individual components.[44,45] In particular, it has been demonstrated that blends of different CPs can enhance the electrical performances of the new materials.[46,47] Therefore, to optimize the conductivity of the CNPs, PPy was added to PEDOT:PSS and MWCNTs doped CNPs. An increase of CNP conductivity of around ten times was observed in the ternary formulation CNPs if compared with the conductivity values of the binary ones. This can be explained considering the high conductivity of PPy domains (10–50 S cm^{-1}, as bulk material)[30] which wraps both cellulose nanofibrils and PEDOT:PSS or MWCNT providing a 3D structure of interconnected pores favoring the transport pathways in the ternary formulations. This effect is enhanced for the PEDOT:PSS-based nanopapers: PPy chains form a conductive network around their core–shell structure which enhances the transport through the bulk of the sample.[30]

For PH500_PPy, the addition of PPy lead to a higher conductivity without significantly increasing the surface roughness, giving a good trade-off between these two parameters. However, the addition of PPy had a negative effect on the morphology of PT2_PPy and MWCNT_PPy nanopapers with an increase in the surface roughness of the ternary formulations probably related to the presence of PPy platelets on the surface of the samples. (Figure S3c,f,i, Supporting Information). In particular, MWCNT_PPy was characterized by the higher surface roughness and the lower compactivity if compared to the other nanopapers (RMSR of around 100 nm). MWCNTs present negative charges from the carboxylic groups which can interact with hydroxyl group of cellulose nanofibrils. Therefore, PPy platelets deposited on both CNF and MWCNT surfaces increase the surface roughness of the composite and make the CNP less compact, probably also as a consequence of the intrinsically weaker PPy–PPy interactions in comparison with cellulose–nanotube, nanotube–nanotube or cellulose–cellulose connections.[28] All of those aspects can be detrimental for the proper operation of the electronic devices fabricated onto it.

Diode structures with degradable characteristics could potentially be used in many different applications, providing continuous operation over predetermined periods of time before dissolving. A degradability test was performed on all the CNP substrates. The substrates were immersed in a phosphate buffer saline (PBS) solution at room temperature (RT). The solution was changed every 24 h and the nanopaper thicknesses were measured after drying them at 60 °C to remove the absorbed water.[48] Figure 2c shows the thickness reduction after 25 days (the thickness values of all the CNPs is reported in Figure S4 in the Supporting Information). After the immersion in PBS, $PT2_{30}$ and $PT2_{50}$ CNPs became extremely fragile and even a soft physical interaction destroyed the substrates by breaking them into small pieces. A 100% reduction of thickness was obtained after 2 days in aqueous solution. The others CNPs reduced their thicknesses by no more than 60% and they did not suffer from any evident structural defects, and nor did they dissolve. Based on these results, PT2 CNPs present interesting features as degradable substrates.

2.2. Characterization of Diodes

As recently demonstrated in our previous work,[37] a barrier-free ohmic contact is observed at the metal/semiconductor

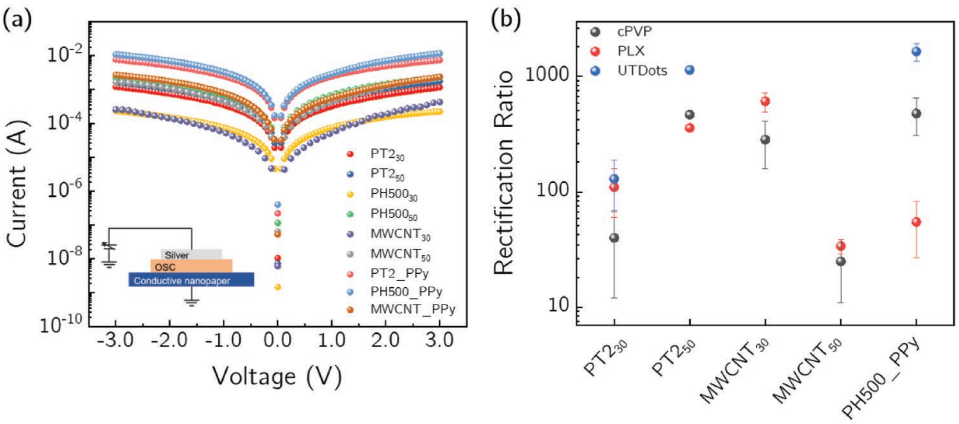

Figure 3. a) Current–voltage characteristic and schematic illustration (inset) of nanopaper/Merck Lisicon SP400/silver junctions. b) Rectification ratio values of the diodes measured at |3 V| reported for different CNPs and dielectrics.

interface, i.e., silver BE/Merck Lisicon SP400 interface. This high-performance amorphous p-type OSC was chosen because its polymeric nature allows an easy control over its deposition and reduces the variability of its electrical behavior due to the absence of a crystallization step.[49] To exclude the presence of an eventual energy barrier at the CNPs/OSC/top electrode (TE) interface, the stack CNPs/Merck Lisicon SP400/silver was fabricated and characterized for each of the different CNPs (see **Figure 3**a, inset). As shown in Figure 3a, all the junctions presented symmetric *I*–*V* characteristics. This can be explained considering the work functions (WFs) of the BEs and TEs: PEDOT:PSS, MWCNT and PPy presented WFs between 4.6 and 5.4 eV[50–52] while the silver top electrode's WF was around 5.2 eV.[37] These values are very similar to the ionization potential of the OSC (5.1–5.3 eV),[37] leading to a negligible energy barrier at both Ag/OSC and OSC/CNPs interfaces. The carriers are free to flow in or out the semiconductor and there is a minimal resistance across the contacts. This confirms the presence of an ohmic contact between the CNPs and the semiconductor. All the CNPs can potentially be used as both substrates and bottom electrodes for the proposed diodes structures: thus, the devices were fabricated using all the different nanopapers (see the Experimental Section for details). As aforementioned, the asymmetric characteristic of a diode is typically related to the fact its resistance is negligible in forward bias and high in reverse bias condition. Organic semiconductor they usually favor solely one type of carriers depending on the ease with which holes or electrons can be injected into the material from the electrodes. Two different regimes of operation can be distinguished: accumulation and depletion, defined according to the effect that the applied voltage has on the semiconductor (Figure S5, Supporting Information). Under the application of a positive voltage to a hole transport semiconductor, free charges are injected into the materials and accumulate at the semiconductor/insulator interface (accumulation region). If a high conductance is registered across the insulator, the accumulation capacitance does not saturate, and a certain amount of current can pass through the insulator (forward bias). Conversely, when a negative bias is applied to the semiconductor, charges accumulate at the electrode/semiconductor interface. Thus, there is no charge at the semiconductor/dielectric interface, leaving only a space charge or depletion layer (reverse bias). The reverse leakage current and forward current give indications about the depletion region and accumulation region at the interface between the semiconductor and the dielectric. The value of the threshold voltage demarcates the switch from one regime to the other.

The diodes were characterized performing impedance-phase angle analysis (*Z*–σ), and current density–voltage (*J*–*V*) to study how the different CNPs affect the deposition of the insulating layer and, consequently, to find the best combination of materials for the CNPs and dielectric to achieve good electrical performances. RR is the ratio of the maximum forward bias current to the maximum reverse bias current recorded when the same absolute voltage is applied to the device (|3 V|). Figure 3b summaries the RR values obtained for diodes fabricated using $PT2_{30}$, $PT2_{50}$, $MWCNT_{30}$, $MWCNT_{50}$, and PH500_PPy CNPs using three inkjet-printed layers of cPVP, three inkjet-printed layers of PLX, and three inkjet-printed layer of UTDots as the insulator for each CNP substrate (the chemical structures of the insulating polymers employed in this work is reported in Figure S6 in the Supporting Information). Even if different layers of cPVP (up to six), PLX (up to three), and UTDots (up to three) were inkjet-printed to increase the film thicknesses, the devices fabricated using $PH500_{30}$, $PH500_{50}$, PT2_PPy, and MWCNT_PPy CNPs resulted in short-circuited structures; probably because of the high RMSR values obtained for these nanopapers (Figure 2b). The electrical characterization of the diodes can be found in Table S1 in the Supporting Information. The lowest RR values (less than 110) were obtained for $PT2_{30}$ and $MWCNT_{50}$ substrates, regardless of the insulator. In particular, $PT2_{30}$ based diodes suffered a low injection at forward bias and $MWCNT_{50}$ based diodes presented high leakage current at reverse voltage (current density values are reported in Table S1 in the Supporting Information). For each CNP substrate, the highest RR value was achieved when UTDots was employed as insulating material (Figure 3b). This increase in electrical performance was due to a higher injection of holes at the forward bias. Interesting RR values of around 1.2×10^3, 6×10^2, and 1.7×10^3 were registered for diodes based on $PT2_{50}$, $MWCNT_{30}$, and PH500_PPy CNPs, respectively. To the best of our knowledge, this work reports the highest RRs obtained for inkjet-printed organic diodes. It is important to emphasize that

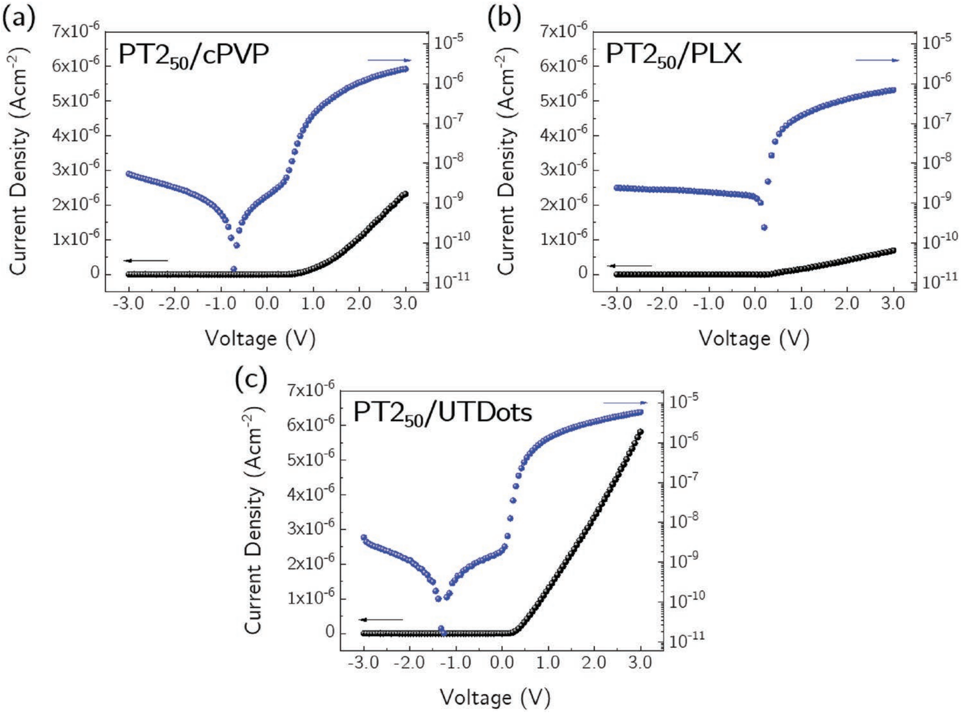

Figure 4. a) Current density/voltage characteristics for PT2$_{50}$/cPVP, b) PT2$_{50}$/PLX, and c) PT2$_{50}$/UTDots in linear scale (left) and semilogarithmic scale (right).

their electrical performances were substantially independent from the CNP conductivities but depended strongly on CNP roughness, which affected the quality of the insulator layers. For this reason, it is preferable to use a CP that can act both as surface planarizer and high-performance conductive filler for the fabrication of conductive CNPs.[43] Additionally, the insulating inkjet-printed PVP, PLX, and UTDots layers contributed to smoothing the substrates significantly lowering any CNP RMSR values (0.4–1.0, 0.6–4, and 2–6 nm, not reported in this work). Thus, rectifying insulator/OSC interface of all diodes was of a good quality with the CNPs/insulator interface responsible for the electrical performance.

Having considered the surface roughness of the substrates, the degradability test and the rectification ratio values obtained, attention will now be focused on the diodes fabricated using PT2$_{50}$ CNPs, whose electrical characterization is reported in **Figure 4** and **Table 1**. Figure 4a refers to PT2$_{50}$/cPVP structures. Even though the phase value in the accumulation region is close to −90 °, the impedance value of these diodes passes from 1270 to 530 MΩ in forward bias, indicating a loss through the insulator. PT2$_{50}$/cPVP presents a maximum forward current density ($J_{\mathrm{f\_MAX}}$) of around 3 μA cm^{-2} and maximum reverse current ($J_{\mathrm{r\_MAX}}$) of around 3 nA cm^{-2}. At V = |3| V, the RR is 470 ± 30. Figure 4b refers to the PT2$_{50}$/PLX structure. Impedance-phase values do not change significantly between forward and reverse region for these diodes, with a phase very close to −90° (−89.9° at −3 V and −87.3° at +3 V). PT2$_{50}$/PLX presents a $J_{\mathrm{f\_MAX}}$ of around 350 nA cm^{-2} and a $J_{\mathrm{r\_MAX}}$ of around 1 nA cm^{-2}. At V = |3 |V, the RR is 360 ± 20. Figure 4c refers to the PT2$_{50}$/UTDots structures. The presence of a leaky insulator is confirmed by the impedance characterization: the impedance value passes from 840 to 510 MΩ in forward bias. However, the phase remains almost constant in both signal bias close to −90° (−88.6° at −3 V and −86.7° at +3 V). PT2$_{50}$/UTDots structures present a $J_{\mathrm{f\_MAX}}$ of around 5 μA cm^{-2} and a $J_{\mathrm{r\_MAX}}$ of around 4 nA cm^{-2}. At V = |3| V, the RR is 1140 ± 84. If compared to the approaches reported so far, the notable RRs of the present work is one order of magnitude higher than the values previously reported for inkjet-printed or paper-based diodes.[37,53–55]

Different conduction mechanisms have been used to demonstrate the carrier transport through insulating films.[56,57] Bulk-limited conduction mechanisms are related to the

Table 1. Current density, impedance and phase values (registered at 1 kHz), and rectification ratios (measured at |3 V|) for PT2$_{50}$/cPVP, PT2$_{50}$/PLX, and PT2$_{50}$/UTDots.

	Reverse bias		Forward bias		Density current at reverse/forward bias [μA cm^{-2}]	RR	Fabrication yield
	Impedance [MΩ]	Phase [°]	Impedance [MΩ]	Phase [°]			
PT2$_{50}$/cPVP	1260	−83	530	−86	(6.4 ± 0.3) 10^{-3}/(3.02 ± 0.06)	470 ± 30	66%
PT2$_{50}$/PLX	20	−90	16	−87	(9.3 ± 0.4) 10^{-4}/(0.35 ± 0.01)	360 ± 20	75%
PT2$_{50}$/UTDots	840	−89	510	−87	(4.5 ± 0.2) 10^{-3}/(5.1 ± 0.1)	1140 ± 84	80%

electrical behavior of the dielectric layer, and include space-charge-limited current (SCLC), Poole–Frenkel (PF) conduction, and hopping conduction. Electrode-limited conduction mechanisms are related to the electrical properties at the electrode/dielectric interface, and include direct tunneling, or Fowler–Nordheim (FN) tunneling, or Schottky conduction. Conduction mechanisms depend on the film composition, film processing, film thickness, energy levels, and densities of traps in the insulator films.[57] Therefore, the determination of the main conduction mechanism could give important information on the physical nature of the charge transport in the dielectric film. The conduction mechanism was determined by evaluating the quality of fit to the current density–voltage data.[56] While going into details of the different conduction mechanisms is outside the aim of this work, to better understand the electrical behavior of the proposed structures, there now follows a brief discussion on the mechanisms of PT2$_{50}$ group. The data fitting from the double-log *J*–*V* curves (**Figure 5**) shows different slopes for different ranges of voltages at forward bias. This is typical of the presence of different transport phenomena in the structures. The slopes (m) of the linear fits of the double-log *J*–*V* characteristics are the exponent in the relation $J\ \alpha\ V^m$. In particular, three distinct regions with three different slopes can be observed. The bending of the curves at high forward bias is typical of bulk-limited conduction mechanisms. PT2$_{50}$/cPVP and PT2$_{50}$/UTDots structures have a slope of 1 ($I\ \alpha\ V^1$) and 0.9 ($I\ \alpha\ V^{0.9}$), respectively, over low voltages (region I in Figure 5a,c). An ohmic mechanism, which is controlled by thermally activated carriers more than by injected carriers,[58] is dominant in this region. Space-charge-limited current/trap-filled-limited (TFL) conduction characterized by $m > 2$, with the filling of the traps exponentially distributed in energy, is obtained at intermediate voltage.[59] Usually, because of the limited mobility values that characterized organic thin films, injected carriers are localized by trap states, producing a space charge that compete with the applied bias and hinders the carrier conduction.[60] The slopes obtained when this mechanism is dominant represent a criterion to compare the stretching of the exponential distribution of carriers: a low slope is typical of an extended distribution, while a high slope is related to an abrupt distribution.[61] In the present study, TFL conduction took place with slopes of 4.8 ($I\ \alpha\ V^{4.8}$) and 2.5, and 3.5 ($I\ \alpha\ V^{2.5,3.5}$) for PT2$_{50}$/cPVP and PT2$_{50}$/UTDots structures, respectively (region II, Figure 5a,c). TFL conduction mechanism with a slope of 5.1 ($I\ \alpha\ V^{5.1}$) can be observed for PT2$_{50}$/PLX diodes at lower voltages (region II, Figure 5b). As these data show, trap-free SCLC is the predominant conduction mechanism for all the structures at high voltages with slopes of 2.4 ($I\ \alpha\ V^{2.4}$), 1.4 ($I\ \alpha\ V^{1.4}$), and 1.6 ($I\ \alpha\ V^{1.6}$) in region III of Figure 5a–c, respectively.

In this region, the majority of the traps are filled by the injected carriers and the accumulation of the charge near the electrodes results in a space charge close to the electrodes. This induces a field that further limits the injection. The current

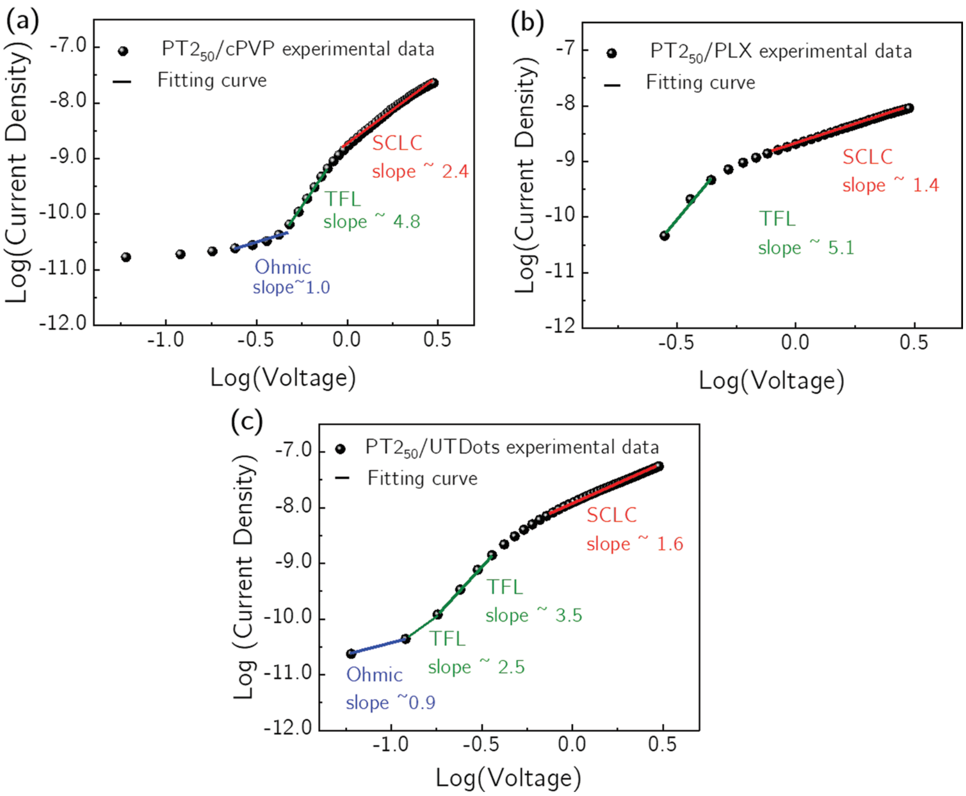

Figure 5. a) Log(current density)–log(voltage) characteristics fitted with straight lines for PT2$_{50}$/cPVP, b) PT2$_{50}$/PLX, and c) PT2$_{50}$/UTDots. The slope of the fitted SCL current is shown.

follows a SCL conduction mechanism, typical of single-carrier devices, according to the relation

$$J = \frac{9}{8}\varepsilon\mu\frac{V_a^2}{L^3} \tag{1}$$

where V_a is the voltage applied to the top electrode, μ is the carrier mobility of the semiconductor, L is the thickness of the semiconductor and ε is permittivity of the semiconductor. Trapped behavior becomes trap-free conduction in region III where there is the transition from TFL curve to Child's law. To quantify the energy barrier, temperature dependent I–V measurements were performed between 243.15 and 343.15 K. Field-assisted thermal emission of carriers over the energy barrier at a metal/insulator interface defines the Schottky conduction. The energy barrier height can be extracted by the slope of the conventional Richardson plot[62]

$$\ln\left(\frac{I_0}{T^2}\right) = \ln\left(AA^*\right) - \frac{q\Phi_B}{kT} \tag{2}$$

where I_0 is the reverse saturation current extrapolated from the straight-line intercept of ln(I) at $V = 0.8$ V. Figure S7 in the Supporting Information reports the characterization for the PT2$_{50}$/UTDots structure. A barrier height of around 0.25 eV was extracted.

2.3. PT2$_{50}$/UTDots Diodes as NO$_2$ Sensors—Proof-of-Concept

Over recent years, the development of gas sensors that can be employed to monitor the air pollution has attracted many research efforts. A paramount prerequisite for public health is the air quality and pollution with toxic gasses has led to diseases in both industrial and developing countries .[63] Nitrogen dioxide (NO$_2$) is one of the predominant pollutant from combusted fuel. Up to the present, commercial NO$_2$ sensors are commonly characterized by high-weight and high-dimensions, present low selectivity, and require high-power supply.[64] Therefore, it is of a great importance to fabricate new light-weight low-power gas sensors that can be mass produced at low-cost with high throughput and correct performance (in terms of high selectivity and sensitivity). Moreover, the possibility to conduct this analysis at RT is of substantial relevance in complicated and often hazardous gaseous environments.[65] Among the chemical sensor devices based on organic semiconductors, diodes present interesting features compared to transistors as they are easier and cheaper to fabricate and simpler to operate. The gas interaction processes lead to a change in the charge carrier mobility of the OSCs that can be easily read through the variation of the output signal of an electronic device. Thus, it is necessary to use a device whose current does not change over time. Figure S8 in the Supporting Information shows the current variation of a PT2$_{50}$/UTDots structure over 90 min and 7 days, respectively. These measurements were taken in ambient conditions to demonstrate the stability of our diodes over the time, before investigating their performance as gas sensors. The setup for the sensing characterization is shown in **Figure 6**a: the tests were carried out on a PT2$_{50}$/UTDots structure, mounted on To-U package, to assess the electrical response of the diodes upon exposure to NO$_2$ gas (see the Experimental Section). Also in this case, the characterization was performed in ambient conditions increasing the gas concentration from 1 to 10 ppm with an incubation time of 50 min before each measurement. As an example, the current variation during the exposure to a 10 ppm concentration of NO$_2$ is reported in Figure S9a in the Supporting Information. The interaction between a p-type OSC and a strong electron acceptor, like NO$_2$, provokes an increase in the number of holes. Therefore, the charge concentration of the semiconductor increases when the diode is exposed to NO$_2$ gas.[66] SP400 is an amorphous polymeric semiconductor that was chosen to improve the gas diffusion and mitigate the problems related to gas absorption–desorption efficiency, typical of OSC characterized by crystal domain boundaries. The induced carriers initially fill the traps under the conduction band and then contribute to the passage of current. The charge carrier mobility is dependent on the carrier concentration as is clearly visible from the variation of the slope of the current–voltage curves (Figure S9b, Supporting Information). The response of the device to NO$_2$ was evaluated using Equation (3)

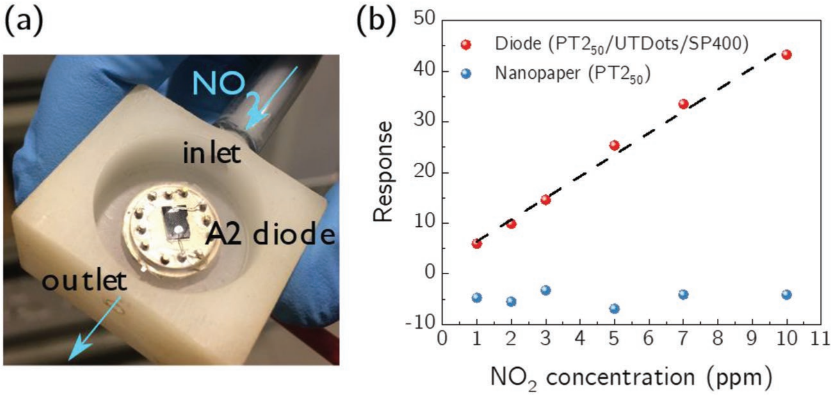

Figure 6. a) Gas sensing setup. b) Response of PT2$_{50}$/UTDots diode structure (red points), and of PT2$_{50}$ nanopaper (blue points) to different concentrations of NO$_2$.

$$\text{Response}\,(\%) = \frac{I_{NO_2} - I_{air}}{I_{air}} \tag{3}$$

where I_{NO_2} and I_{air} are the maximum forward currents of the sensor measured in presence of NO$_2$ and in dry air, respectively. Figure 6b shows a linear correlation between the response and the NO$_2$ concentration from 1 to 10 ppm (red points). From its slope the device sensitivity was determined to be 4% ppm^{-1}. The same test performed on the PT2$_{50}$/UTDots nanopaper (blue points) did not show any significant current variation. This result confirms that the active component in the NO$_2$ sensing is the organic semiconductor and not the CNP. After stopping the NO$_2$ flow, the current of the diode started to decrease and approached the original current level after

120 min, which was found to be the recovery time of the diode gas sensor. The sensing performance of the devices regarding to sensitivity (for ultralow concentrations, ppb level) and selectivity will be object of future investigations and optimizations. However, this preliminary test should be considered as a proof-of-concept of feasible applications of the diodes.

3. Conclusion

Novel high-performing organic diodes onto conductive cellulose substrates were fabricated by inkjet-printing and characterized. Different polymeric and carbon-based conductive fillers were evaluated to provide conductivity to cellulose substrates. Best performance was obtained by the polymeric filler PT2 since those CNPs possessed an extremely smooth surface and good conductivity. Organic diodes with fabrication yield of around 80% showed outstanding electrical behavior when cellulose substrates containing PT2 acted as both substrate and bottom electrode and UTDots was employed as insulator. Rectification ratio of up to 1.2×10^3 with negligible reverse current and a current density of 5.1 μA cm^{-2} at forward bias with a reproducibility of 90% were obtained in ambient conditions. Thermionic emission model was found to be the main conduction mechanisms responsible for carrier injection into the insulator. From temperature-dependent characterizations, it is possible to assume a barrier height at semiconductor/insulator interface of 0.25 eV.

Finally, CNPs diodes demonstrated to interact successfully with the NO_2 gas and reached a sensing response of 4% ppm^{-1} operating at room temperature. This test is presented as a proof-of concept for the possible sensing applications of these structures.

4. Experimental Section

Materials: High-purity softwood cellulose pulp was provided by Domsjö (Sweden) and used as cellulose raw material. 98% pure pyrrole was purchased from Sigma Aldrich and was used for the chemical synthesis of PPy. Aqueous solutions of 1.1 wt% of two different types of PEDOT:PSS (Clevios PT2 and PH500), containing 1:2.5 by weight of each component, were purchased from Clevios Heraeus Deutschland (Leverkusen, Germany). MWCNTs from Sigma Aldrich containing more than 95% of carbon with an outside diameter and length of 6–9 nm × 5 µm were treated with H_2SO_4/HNO_3 (3:1) reaction mixture prior to use. Iron (III) chloride ($FeCl_3$), Tween-80, 2,2,6,6-tetramethyl-1-1-piperidinyloxy (TEMPO), sodium bromide (NaBr), sodium hypochlorite (NaClO), HCl, NaOH, NaCl, H_2SO_4, and HNO_3 were purchased from Sigma Aldrich and used without further purification. For the diode fabrication, poly(4-vinylphenol, PM 25000) (cPVP), poly(melamine-*co*-formaldehyde) methylated (CL), and propylene glycol methyl ether acetate (PGMEA) were purchased from Sigma Aldrich and used without further purification. The Epoxy ink is the Prielex SU-8 ink (PLX) from MicroChem. The high-K epoxy insulator (UTDots) is a commercial ink from UTDots, Inc., that contains amorphous silica nanoparticles, epoxy resin, and epoxy hardener. The OSC Lisicon SP400 is a commercial hole transport amorphous semiconductor from Merck. The top silver electrode (TE) is a silver conductive paste from Electrolube.

Preparation of the Nanopapers: Figure S1 in the Supporting Information reports all the different CNPs fabricated in this work. The preparation of CNF followed the TEMPO-mediated oxidation at basic pH described in previous work[67] with 5 mmol of NaClO until constant pH of 10. After TEMPO-oxidation, the cellulose suspension was filtered and washed five times with distilled water to remove all nonreacted reagents and free ions. After that, the cellulose suspension at 1.1 wt% concentration was passed through a high-pressure homogenizer (NS1001L PANDA PLUS 2K_GEA), three times at each pressure of 300, 600, and 900 bars. For the preparation of CNPs, the CNF was diluted to 0.2 wt% concentration with distilled water, dispersed for 30 s by means of an ultraturrax (IKA, GmbH& Co. KG, Germany) and sonicated, for 10 min at an amplitude of 60% in two equal intervals with a 2 min standby, using a Q700 sonicator. For the fabrication of CNF-PEDOT:PSS nanopapers, two different types of PEDOT:PSS were used: PT2 and PH500. The conductive polymers were also diluted with distilled water to 0.5 wt% and stirred for 5 min. The PEDOT:PSS suspensions were added into the above CNF suspension with different proportions of CNF-PEDOT:PSS (70/30 and 50/50). The mixture was stirred for 1 h, filtered with a vacuum filter, and dried for 20 min at 85 °C under a pressure of 0.5–0.6 bar using a Rapid Köthen sheet dryer. The samples were labeled according to the proportion of the conductive polymer: $PT2_{30}$, $PT2_{50}$, $PH500_{30}$ and, $PH500_{50}$. For the fabrication of CNF-MWCNT nanopapers, prior to use, the MWCNTs were submitted to surface oxidation to get the solubility in water, following a procedure reported in a previous work.[29] After that, the CNF suspension at 0.2 wt% was prepared following the procedure described above. MWCNTs were dispersed in distilled water (1 mg mL^{-1}) using the ultra turrax (IKA, GmbH& Co. KG, Germany) for 3 min. Different amounts of MWCNT (30 and 50 wt% with respect to CNF content) were added dropwise into the CNF suspension. The CNF-MWCNT mixture was stirred for 24 h at room temperature to obtain a homogenous distribution of MWCNT in the CNF network. The CNF-MWCNT suspension was then filtered overnight using a vacuum filter and dried using the same procedure described for the CNF-PEDOT:PSS nanopapers. Also in this case, the samples were labeled according to the proportion of the MWCNTs: $MWCNT_{30}$, and $MWCNT_{50}$.

For the preparation of the ternary nanopapers, PEDOT:PSS suspension and MWCNT dispersion were prepared according to the procedure reported above. 0.21 mL of pyrrole monomer were mixed with 30 mL of HCl (0.5 M). The pyrrole acidic solution was added to the CNF suspension and the mixture was stirred for 5 min. A solution of 1.21 g of $FeCl_3$ in 30 mL of HCl (0.5 M) was added drop by drop into the suspensions to initiate the polymerization of the pyrrole. The final mixture was kept under stirring for 1 h, filtered with a vacuum filter, and subsequently washed with 500 mL of HCl 0.5 M, 500 mL of NaCl 0.1 M, and 500 mL of distilled water. During the last wash with the distilled water, the solution was sonicated for 2 min to remove the eventual presence of gas and to promote the homogenization. Finally, the nanopapers were dried using the same procedure described for the binary CNPs. The samples were labeled according to the components: PT2_PPy, PH500_PPy, and MWCNT_PPy.

Fabrication of the Diodes: Figure 1a shows the fabrication scheme of the diode structures presented in this work. Optical image of the fabricated device is presented in Figure 1bi and SEM image of the diode can be observed in Figure 1bii. The same procedure was followed for the fabrication of all the structures. A Fujifilm Dimatix DMP2831 desktop printer was used as the printing setup. In this work, three different polymeric insulators were directly inkjet-printed onto CNPs. A solution of PVP and CL in PGMEA (the concentrations of PVP and CL were 90 and 45 mg mL^{-1}) was inkjet-printed using a drop spacing (DS) of 30 µm while keeping the substrate at room temperature. Crosslinking was performed in an oven for 30 min at 150 °C. The diodes fabricated with inkjet-printed cPVP layers have a thickness of 1.0 ± 0.1 µm. PLX SU-8 ink was patterned using a DS of 40 µm and keeping the temperature platen at 45 °C and the temperature of the printhead at 45 °C. The curing process involved a UV treatment for 30 s. The diodes fabricated with inkjet-printed PLX layers have a thickness of 3.7 ± 0.1 µm. The high-K epoxy insulator UTDots was printed using a DS of 25 µm and heating the platen at 45 °C. The curing procedure was carried out on a hot plate at 150 °C for 60 min. The diodes fabricated with inkjet-printed UTDots layers have a thickness of 7.8 ± 0.6 µm. The OSC was deposited on the top of the dielectric layer using drop casting (0.1 µL). The curing process was performed on a hot plate for 2 min at 100 °C. The silver TE was deposited by means of drop casting and dried in air.

The diodes are named according to the type of nanopaper and the type of dielectric employed. The left part of the label indicates the CNF used and the right part indicates the insulating layer, for example: PT2$_{30}$/cPVP diodes.

Device Characterization: The morphological and electrical characterizations were carried out on at least three samples of 0.5 cm × 2.0 cm area per each nanopaper (AFM images were performed over 5 µm × 5 µm areas). The electrical conductivity of the nanopapers was determined following the procedure reported by Lay et al. in 2016.[29] The current–voltage characterizations of the diodes were carried out using an Agilent B1500A Semiconductor Analyzer. Impedance measurements were performed with an Agilent 4294A Precision Impedance Analyzer. All the electrical measurements were performed in ambient conditions and ambient light. Micrographs were acquired using a light microscope DM4000 from Leica and scanning electron microscopy images were obtained using a Carl Zeiss Leo 1530 E-beam instrument. Atomic force microscopy images were carried out using the Nanoscope Veeco Dimension 3100. The response of the diodes to nitrogen dioxide was recorded using a homemade stainless-steel chamber of 8.6 mL volume connected to a Gometrics MGP2 gas mixer with four Bronkhorst mass-flow controllers. Electrical characterization of gas sensors was carried out with Keithley 2602A dual source measure units and flowing gas concentrations were controlled using an in-house application developed on Labview software. For all the gas measurements, a constant flow of 200 mL min^{-1} was maintained.

Supporting Information

Supporting Information is available from the Wiley Online Library or from the author.

Acknowledgements

This work was supported by MICIU-Spain (project RTI2018-102070-B-C21), Generalitat de Catalunya (project 2017SGR-1159) and by FEDER funds. Fellowship for the transfer and innovation was given by the University of Girona to BIMATEC Group through Alex Espígol, Eng. (ref. BTI2018/12). The authors would like to thank the R&D partners: Fujifilm Dimatix, Ceradrop, and Merck for providing with the research related consumables and their technical details.

Conflict of Interest

The authors declare no conflict of interest.

Author Contributions

The manuscript was written through contributions of all authors. All authors have given approval to the final version of the manuscript.

Keywords

cellulose nanofibers, conductive nanopapers, inkjet-printing, organic diodes, rectification ratios

Received: September 5, 2019
Revised: November 4, 2019

[1] M. Irimia-Vladu, E. D. Głowacki, G. Voss, S. Bauer, N. S. Sariciftci, *Mater. Today* **2012**, *15*, 340.
[2] M. (Mihai) Irimia-Vladu, E. D. Glowacki, N. S. Sariciftci, S. Bauer, *Green Materials for Electronics*, Wiley-VCH Verlag GmbH & Co. KGaA, Weinheim, Germany **2017**.
[3] R. K. Mishra, S. K. Ha, K. Verma, S. K. Tiwari, *J. Sci. Adv. Mater. Devices* **2018**, *3*, 263.
[4] D. Tobjörk, R. Österbacka, *Adv. Mater.* **2011**, *23*, 1935.
[5] Y. Zhang, L. Zhang, K. Cui, S. Ge, X. Cheng, M. Yan, J. Yu, H. Liu, *Adv. Mater.* **2018**, *30*, 1801588.
[6] M. Nogi, S. Iwamoto, A. N. Nakagaito, H. Yano, *Adv. Mater.* **2009**, *21*, 1595.
[7] F. Hoeng, A. Denneulin, J. Bras, *Nanoscale* **2016**, *8*, 13131.
[8] R. K. Mishra, A. Sabu, S. K. Tiwari, *J. Saudi Chem. Soc.* **2018**, *22*, 949.
[9] U. Zschieschang, H. Klauk, *J. Mater. Chem. C* **2019**, *7*, 5522.
[10] Y. Z. Zhang, Y. Wang, T. Cheng, W. Y. Lai, H. Pang, W. Huang, *Chem. Soc. Rev.* **2015**, *44*, 5181.
[11] Y. H. Jung, T. H. Chang, H. Zhang, C. Yao, Q. Zheng, V. W. Yang, H. Mi, M. Kim, S. J. Cho, D. W. Park, H. Jiang, J. Lee, Y. Qiu, W. Zhou, Z. Cai, S. Gong, Z. Ma, *Nat. Commun.* **2015**, *6*, 7170.
[12] A. Malti, J. Edberg, H. Granberg, Z. U. Khan, J. W. Andreasen, X. Liu, D. Zhao, H. Zhang, Y. Yao, J. W. Brill, I. Engquist, M. Fahlman, L. Wågberg, X. Crispin, M. Berggren, *Adv. Sci.* **2016**, *3*, 1500305.
[13] D. Ha, Z. Fang, N. B. Zhitenev, *Adv. Electron. Mater.* **2018**, *4*, 1700593.
[14] D. Gaspar, S. N. Fernandes, A. G. De Oliveira, J. G. Fernandes, P. Grey, R. V. Pontes, L. Pereira, R. Martins, M. H. Godinho, E. Fortunato, *Nanotechnology* **2014**, *25*, 094008.
[15] S. Dai, Y. Chu, D. Liu, F. Cao, X. Wu, J. Zhou, B. Zhou, Y. Chen, J. Huang, *Nat. Commun.* **2018**, *9*, 2737.
[16] P. Tammela, Z. Wang, S. Frykstrand, P. Zhang, I.-M. Sintorn, L. Nyholm, M. Strømme, *RSC Adv.* **2015**, *5*, 16405.
[17] R. Martins, I. Ferreira, E. Fortunato, *Phys. Status Solidi RRL* **2011**, *5*, 332.
[18] E. Fortunato, N. Correia, P. Barquinha, L. Pereira, G. Goncalves, R. Martins, *IEEE Electron Device Lett.* **2008**, *29*, 988.
[19] T. Öhlund, J. Örtegren, S. Forsberg, H.-E. Nilsson, *Appl. Surf. Sci.* **2012**, *259*, 731.
[20] U. Zschieschang, T. Yamamoto, K. Takimiya, H. Kuwabara, M. Ikeda, T. Sekitani, T. Someya, H. Klauk, *Adv. Mater.* **2011**, *23*, 654.
[21] C. Y. Wang, C. Fuentes-Hernandez, W. F. Chou, B. Kippelen, *Org. Electron. Phys. Mater. Appl.* **2017**, *41*, 340.
[22] H. Fukuzumi, T. Saito, Y. Okita, A. Isogai, *Polym. Degrad. Stab.* **2010**, *95*, 1502.
[23] Y. Fujisaki, H. Koga, Y. Nakajima, M. Nakata, H. Tsuji, T. Yamamoto, T. Kurita, M. Nogi, N. Shimidzu, *Adv. Funct. Mater.* **2014**, *24*, 1657.
[24] H. Sirringhaus, *Adv. Mater.* **2014**, *26*, 1319.
[25] S. Conti, S. Lai, P. Cosseddu, A. Bonfiglio, *Adv. Mater. Technol.* **2017**, *2*, 1600212.
[26] A. Teichler, J. Perelaer, U. S. Schubert, *J. Mater. Chem. C* **2013**, *1*, 1910.
[27] M. Caironi, Y.-Y. Noh, *Large Area and Flexible Electronics*, Wiley-VCH Verlag GmbH & Co. KGaA, Weinheim, Germany **2015**, p. 592.
[28] M. Lay, J. A. Méndez, M. À. Pèlach, K. N. Bun, F. Vilaseca, *Cellulose* **2016**, *23*, 3925.
[29] M. Lay, J. A. Méndez, M. Delgado-Aguilar, K. N. Bun, F. Vilaseca, *Carbohydr. Polym.* **2016**, *152*, 361.
[30] M. Lay, M. À. Pèlach, N. Pellicer, J. A. Tarrés, K. N. Bun, F. Vilaseca, *Carbohydr. Polym.* **2017**, *165*, 86.
[31] C. Ding, X. Qian, J. Shen, X. An, *BioResources* **2010**, *5*, 303.
[32] G. A. Snook, P. Kao, A. S. Best, *J. Power Sources* **2011**, *196*, 1.
[33] C. J. Hawker, *Science* **2005**, *309*, 1200.

[34] S. Yun, J. Kim, *Smart Mater. Struct.* **2007**, *16*, 1471.
[35] L. Deng, R. J. Young, I. A. Kinloch, A. M. Abdelkader, S. M. Holmes, D. A. De Haro-Del Rio, S. J. Eichhorn, *ACS Appl. Mater. Interfaces* **2013**, *5*, 9983.
[36] A. Hajian, Z. Wang, L. A. Berglund, M. M. Hamedi, *Adv. Electron. Mater.* **2019**, *5*, 1800924.
[37] C. Martínez-Domingo, S. Conti, L. Terés, H. L. Gomes, E. Ramon, *Org. Electron.* **2018**, *62*, 335.
[38] M. Robin, W. Kuai, M. Amela-Cortes, S. Cordier, Y. Molard, T. Mohammed-Brahim, E. Jacques, M. Harnois, *ACS Appl. Mater. Interfaces* **2015**, *7*, 21975.
[39] K. Y. Mitra, M. Polomoshnov, C. Martínez-Domingo, D. Mitra, E. Ramon, R. R. Baumann, *Adv. Electron. Mater.* **2017**, *3*, 1700275.
[40] A. B. Kaiser, G. Düsberg, S. Roth, *Phys. Rev. B* **1998**, *57*, 1418.
[41] L.-L. Chua, P. K. H. Ho, H. Sirringhaus, R. H. Friend, *Adv. Mater.* **2004**, *16*, 1609.
[42] N. J. Kaihovirta, D. Tobjörk, T. Mäkelä, R. Österbacka, *Appl. Phys. Lett.* **2008**, *93*, 053302.
[43] T. Sekitani, U. Zschieschang, H. Klauk, T. Someya, *Nat. Mater.* **2010**, *9*, 1015.
[44] J. Wang, J. Dai, T. Yarlagadda, *Langmuir* **2005**, *21*, 9.
[45] B. Zhang, Y. Xu, Y. Zheng, L. Dai, M. Zhang, J. Yang, Y. Chen, X. Chen, J. Zhou, *Nanoscale Res. Lett.* **2011**, *6*, 431.
[46] E. Andreoli, K.-S. Liao, A. Haldar, N. J. Alley, S. A. Curran, *Synth. Met.* **2013**, *185–186*, 71.
[47] J. Li, Y. Du, R. Jia, J. Xu, S. Shen, *Materials* **2017**, *10*, 780.
[48] S.-K. Kang, S.-W. Hwang, S. Yu, J.-H. Seo, E. A. Corbin, J. Shin, D. S. Wie, R. Bashir, Z. Ma, J. A. Rogers, *Adv. Funct. Mater.* **2015**, *25*, 1789.
[49] G. Grau, V. Subramanian, *Adv. Electron. Mater.* **2016**, *2*, 1500328.
[50] W. S. Su, T. C. Leung, C. T. Chan, *Phys. Rev. B* **2007**, *76*, 235413.
[51] A. M. Nardes, M. Kemerink, M. M. de Kok, E. Vinken, K. Maturova, R. A. J. Janssen, *Org. Electron.* **2008**, *9*, 727.
[52] O. Inganäs, T. Skotheim, I. Lundström, *J. Appl. Phys.* **1983**, *54*, 3636.
[53] Y. Liu, T. Cui, *Macromol. Rapid Commun.* **2005**, *26*, 289.
[54] K. Y. Mitra, C. Sternkiker, C. Martínez-Domingo, E. Sowade, E. Ramon, J. Carrabina, H. L. Gomes, R. R. Baumann, *Flexible Printed Electron.* **2017**, *2*, 015003.
[55] A. G. Martinez-Lopez, W. Y. Padron-Hernandez, D. Pourjafari, G. Oskam, G. Rodriguez-Gattorno, M. Estrada, J. C. Tinoco, *IEEE Electron Device Lett.* **2018**, *39*, 1940.
[56] T. W. Hickmott, *J. Appl. Phys.* **2005**, *97*, 104505.
[57] P. Stallinga, *Electrical Characterization of Organic Electronic Materials and Devices*, John Wiley & Sons, Ltd, Chichester, UK **2009**.
[58] Y. S. Ocak, M. Kulakci, T. Kiliçoğlu, R. Turan, K. Akkiliç, *Synth. Met.* **2009**, *159*, 1603.
[59] D. F. Barbe, *J. Phys. D: Appl. Phys.* **1971**, *4*, 427.
[60] P. Mark, W. Helfrich, *J. Appl. Phys.* **1962**, *33*, 205.
[61] D. S. Shang, Q. Wang, L. D. Chen, R. Dong, X. M. Li, W. Q. Zhang, *Phys. Rev. B: Condens. Matter Mater. Phys.* **2006**, *73*, 245427.
[62] A. Shetty, B. Roul, S. Mukundan, L. Mohan, G. Chandan, K. J. Vinoy, S. B. Krupanidhi, *AIP Adv.* **2015**, *5*, 097103.
[63] K. Wetchakun, T. Samerjai, N. Tamaekong, C. Liewhiran, C. Siriwong, V. Kruefu, A. Wisitsoraat, A. Tuantranont, S. Phanichphant, *Sensors Actuators, B Chem.* **2011**, *160*, 580.
[64] A. R. Jalil, H. Chang, V. K. Bandari, P. Robaschik, J. Zhang, P. F. Siles, G. Li, D. Bürger, D. Grimm, X. Liu, G. Salvan, D. R. T. Zahn, F. Zhu, H. Wang, D. Yan, O. G. Schmidt, *Adv. Mater.* **2016**, *28*, 2971.
[65] C. Zhang, P. Chen, W. Hu, *Chem. Soc. Rev.* **2015**, *44*, 2087.
[66] A. Lv, Y. Pan, L. Chi, *Sensors* **2017**, *17*, 213.
[67] H. Fukuzumi, T. Saito, T. Iwata, Y. Kumamoto, A. Isogai, *Biomacromolecules* **2009**, *10*, 162.